# Droplet impact on liquid films: bouncing-to-merging transitions for two-liquid systems

Xian Wu and Abhishek Saha\*

Department of Mechanical and Aerospace Engineering,

University of California San Diego, La Jolla, CA-92093, USA

(Dated: January 30, 2023)

The dynamics of a liquid droplet impacting a liquid film of different compositions is critical for many industrial processes, including additive manufacturing and bio-printing. We, herein, present an exposition of droplet impact on liquid films investigating the effects of mismatch in their properties on bouncing to merging transitions. Experiments are conducted for two sets of liquid combinations, namely alkanes and silicon oils. The regime maps for impact outcomes (bouncing vs. merging) are created from detailed experiments with various single and two-liquid systems. The results highlight that the two-liquid systems exhibit an additional merging regime, which is not observed for single-liquid systems. Subsequently, the scaling analyses for transitional boundaries between various regimes are revisited, and new scaling laws are proposed to include the effects of asymmetry in the droplet and film properties. Finally, the experimental results are used to assess the performance of the proposed scaling laws.

### I. INTRODUCTION

Droplet impact on the liquid film is ubiquitous in many natural and industrial systems. For example, the impact of rain droplets on seawater and associated breakup, bubble entrapment, and mixing results in the passive transport of minerals and gases from air to sea and vice versa, which is critically essential for the survival of marine life. In 2-Dimensional (2D) and 3-Dimensional (3D) inkjet printing, the impacts of ink droplets on the substrates wetted by previously deposited droplets and subsequent spreading, drying, and mixing control the resolution of the prints and strength of the structures. Similarly, in tissue engineering and bio-printing applications, control of the adhesion and separation of impacting droplets with the impacted wetted gelled substrate is imperative in achieving the targeted morphology of the cellular structures. Due to its criticality in many engineering and natural systems, droplet impact on liquid film has been studied extensively in a wide range of conditions when the film thickness is significantly larger than the droplet size. A major volume of research focused on the impact dynamics and associated deformation and instability in the interface, resulting in events like jetting, splashing, crown formation, crater formation, etc. [1–10] Some of the studies also highlighted the interfacial mixing of the droplet and the film through vortex formation and post-impact bubble entrapment. [11–15] Recently, researchers have also investigated the spreading and rebounding of compound droplets (containing air bubble in a liquid droplet) when impacted on solid and liquid surfaces. [16–19]1 The major advances in the field of droplet impact have been periodically summarized in reviews by Rein [1], Yarin [20], Josserand and Thoroddsen [21].

While the dynamics mentioned above frequently occur during impact, where the droplet coalesces or merges with the film, some studies have highlighted that impacts can also lead to non-coalescence or bouncing. During the impact process, the droplet and the film interfaces trap a microscopic gas layer, which evolves as the droplet approaches the film [5, 22–24]. When the impact inertia is strong enough to squeeze the gas layer, the droplet and film interfaces come close enough for molecular (van der Waals) forces to institute merging or coalescence. This is why bouncing is generally observed for low-velocity impacts. Previous experiments by us [24–26] and others [27–30] have conclusively demonstrated that the transition from bouncing to merging depends on both Weber number,  $We = 2\rho U^2 R/\sigma$  and normalized film thickness,  $H^* = H/R$ . Here,  $\rho$  is the liquid density,  $\sigma$  is the liquid-air surface tension, R is the droplet radius, U is the impact velocity, and H is the film thickness. Tang et al. [25] showed that when the film thickness  $(H^*)$  becomes smaller than a critical value, the impact is affected by the solid substrate under the film, and as such, bouncing-to-merging transitions for impacts on a deep pool  $(H^* >> 1)$ , an intermediate film  $(H^* \approx 1)$  and a thin film  $(H^* << 1)$  are characteristically different. He et al. [31] showed that the deformability of the ultra-thin films  $(H^* < 0.1)$  alters the bouncing dynamics and drainage of the gas layer. In a recent study [32], we have highlighted that the softness of the substrate below the liquid film can also affect the transition by absorbing some of the impact energy.

The above summary outlines the volume of research on droplet impacts on liquid films, where the droplet and film are of the same liquid. However, the composition of the droplet and the impacted film are drastically different in many

<sup>\*</sup> email: asaha@eng.ucsd.edu

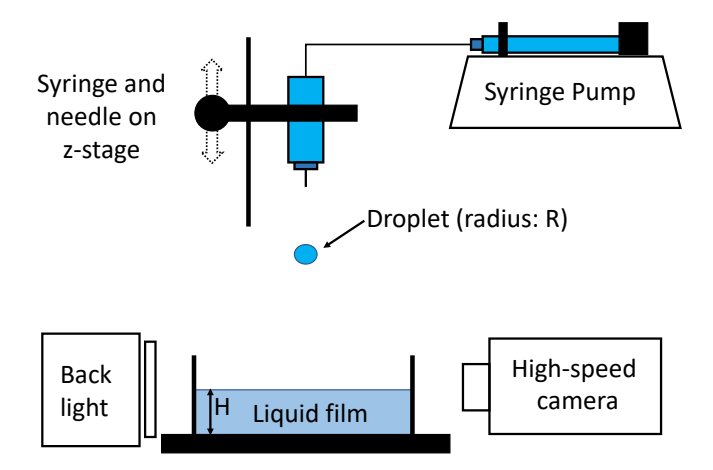


FIG. 1: The schematic diagram of the experimental setup used for the droplet impact study (drawn not to scale).

applications. For example, the ink droplets land on a substrate covered with a second liquid in 3D printing and tissue printing applications. As such, the inhomogeneity in the properties of droplets and film becomes a critical factor in the ensuing impact dynamics. However, only a few investigations systematically studied the asymmetry in the properties of the droplet and the film. Among them, Che and Matar [33] looked into the impact of droplets on immiscible liquid films. In their experiments, they observed the formation of a compound crown followed by a central jet when a water droplet impacts the oil film. However, for the opposite scenario, when oil droplets impacted the water film, a rapid spread on the film surface reduced the chances of crown formation. Langley and Thoroddsen [34] reported rebound for low Weber numbers using large-viscosity drop on low-viscosity liquid film. They also found that the large-viscosity droplet delays the rupture of the interfacial gas layer and exhibits different rupture dynamics. Recently, Wang et al. [35] analyzed the balance of interfacial tensions in a water droplet that impacted an oil layer to understand the dynamics of immiscible liquids. They highlighted that the interfacial tension balance is well maintained along the triple line because of a low capillary number. Furthermore, they proposed a semi-empirical relation to describe the transition between the regimes of non-penetration and penetration, which shows a weak dependence on viscosity. By numerical simulations, Liu et al. [36] investigated the dynamics of the droplet impact on a film of a separate liquid with horizontal velocity. By fixing the density ratio (droplet to film), they showed that the Bond number ( $Bo = \Delta \rho q R/\sigma$ ) plays a critical role in penetration along with the Weber number (We) and the dimensionless film thickness  $(H^*)$ . Here,  $\Delta \rho$  is the density difference between the droplet and the film liquids.

The review of recent work on droplet impact involving binary liquids highlights that studies on the detailed dynamics of miscible liquids still need to be completed. Only some aspects of the dynamics were studied in great detail for immiscible liquids. Recognizing this knowledge gap, we present an experimental investigation of droplet impact on liquid films with various thicknesses involving binary miscible liquid systems. The primary goal is to explore the impact dynamics in the low We regime, where bouncing-to-merging transitions occur, and to highlight any morphological differences compared to single-liquid systems. Furthermore, we want to extend the scaling analyses for regime boundaries presented for single-liquid systems to arrive at modified scaling laws incorporating the asymmetry in droplet and liquid properties. Finally, we will test whether modified scaling can work with data from single and binary liquid system experiments to see its efficacy.

### II. EXPERIMENTAL SETUP

The schematic of the experimental setup used in the study is shown in Figure 1. The droplets were generated by pushing the liquid through a vertically mounted needle using a syringe pump at a constant flow rate. The flow rate of the syringe pump was maintained to be small enough such that only a single droplet was created. When the droplet becomes large enough to overcome the capillary force, it detaches from the needle and lands on the liquid film hosted inside a glass container with a  $25 \text{mm} \times 25 \text{mm}$  cross-section directly placed under the needle. The impact process was imaged by a high-speed monochromatic camera (Phantom V7.3) connected with a 50 mm Nikon lens and an extension below. A high-intensity diffused halogen light provided the back-lighting. The images were recorded at about 15000 frames per second, with a spatial resolution of 55 pixels/mm. The impact velocity (U) was modulated by changing the needle's height from the impacted liquid surface. From high-speed images, U was calculated based on the time

	Liquid	$\rho \; (\mathrm{kg/m^3})$	$\sigma  (\rm mN/m)$	$\nu$ (cSt)
Alkanes	n-decane (C10)	730	24.55	2.37
	n-tetradecane (C14)	767	26.50	3.60
	S3	898	18.3	3.00
Silicon Oils	S4.5	898	18.16	4.50
	S20	950	20.07	20.0

TABLI

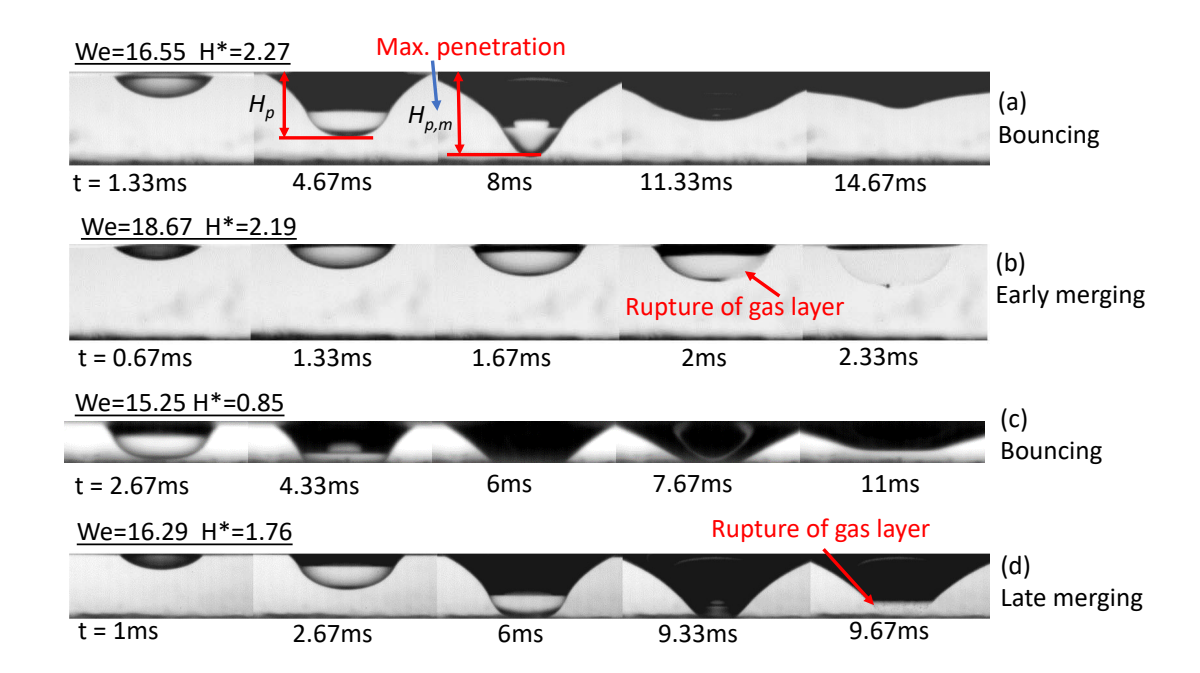


FIG. 2: The side view of different impact outcomes from droplet impact on a liquid film experiment in a single-liquid system. (a) Bouncing on a deep pool (We=16.55, H\*=2.27). (b) Early merging on a deep pool (We=17.67 H\*=2.19). (c) Bouncing on a shallow pool (We=15.25 H\*=0.85). (d) Late merging on a shallow pool (We=16.29 H\*=1.76).

derivative of the distance traveled by the droplet centroid before the impact. The film thickness (H), controlled by adding or withdrawing liquid from the chamber, was measured directly from the images before each experiment. The glass chamber was cleaned, and the film was replaced regularly after five to ten experiments to ensure the film was free from significant contamination. This was particularly necessary for experiments with binary liquid systems since the accumulation and mixing of the droplet with the film can modify the properties of the latter. This study used five liquids from two different liquid groups, alkanes, and silicon oils. The properties of individual liquids are listed in Table I. For experiments with a binary liquid system, combinations from the same liquid groups were used, as discussed in the results sections.

We will present results from both single and binary liquid systems. To identify and distinguish these systems, we used the following terminology. In single-liquid experiments, where a droplet of liquid 'L1' impacts the film of the same liquid 'L1', we will identify the system as 'L1-L1'. In a binary liquid system, where a liquid 'L1' droplet impacts a liquid 'L2' film, we will use the symbol 'L1-L2'. Furthermore, the properties of the droplet and the film will be identified with subscripts "d" and "f", respectively. For example,  $\rho_d$ ,  $\mu_d$ ,  $\nu_d$ , and  $\sigma_d$  are density, dynamic viscosity, kinematic viscosity, and surface tension of the droplet liquid. We also note that we will define the impact Weber number,  $We = 2\rho_d U^2 R/\sigma_d$ , based on droplet properties.

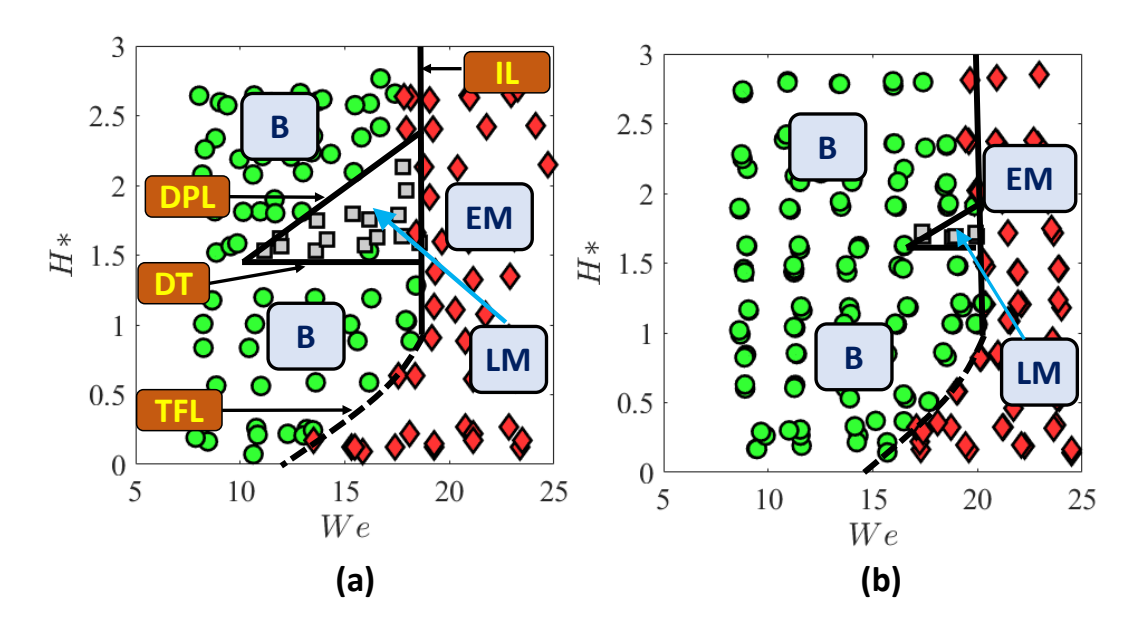


FIG. 3: The regime diagrams of droplet impact outcomes for single-liquid systems (a) S3-S3, (b) S4.5-S4.5. The transition boundaries between different impact outcomes are shown in black lines. B: Bouncing, EM: Early merging, LM: Late merging. IL: inertial Limit, TFL: Thin Film Limit, DT: Deformation Transition, and DPL: Deep Pool Limit.

### III. RESULTS AND DISCUSSION

### A. Global Dynamics

## 1. Single-Liquid System

Although the primary focus of the present study is the binary systems, just so you know, we will first discuss the outcomes from single-liquid systems. We will also provide physical descriptions of various impact outcomes. The bouncing-to-merging dynamics for single-liquid systems have been extensively discussed in our previous studies [25–27].

The high-speed images of typical impact processes at various We and  $H^*$  are shown in Fig. 2 for the S3-S3 system. The bouncing and merging outcomes can be presented in a normalized film thickness  $(H^* = H/R)$  vs. Weber number (We) plot, generally called the regime diagram. In Fig. 3, we present the regime diagrams for single-liquid systems (S3-S3 and S4.5-S4.5), constructed by observing the impact outcomes during repeated experiments performed at various We and  $H^*$  conditions. Next, we will discuss the various impact dynamics observed in single-liquid systems.

At larger  $H^*$ , when We is below a critical value (< 18 for S3-S3 and < 20 for S4.5-S4.5), the impacted droplet deforms and penetrates the film surface without breaking the interfacial gas layer. After the impact, the deformation of the film continues to grow until the maximum penetration depth is reached (t=8 ms in Fig. 2a). Here, the  $H^*$  is large enough to ensure that the thickness of the film would not limit the penetration of the droplet. At the end of the penetration process or the approaching stage, the initial kinetic energy of the droplet is lost as the surface energy in the deformed liquid film, the kinetic energy of the flow created in the liquid film, and the viscous dissipation. Subsequently, the deformed film relaxes due to capillarity, and in the process, it pushes the droplet. In this rebounding stage, both the film and the droplet move upward, causing the droplet to bounce. It was previously shown for droplet-droplet [37, 38], droplet-film [25, 27] and jet-jet [39, 40] collisions, that the success or failure in achieving merging depends on the initial kinetic energy, which brings the interfaces closer, against the resistance provided by the interfacial microscopic gas layer. In this regime of low We, the impact kinetic energy of the droplet is not strong enough to squeeze the gas layer. Hence, bouncing is observed.

However, when We is increased beyond the critical value, the impact inertia becomes strong enough to squeeze the gas layer and to bring the droplet and film interfaces close enough for molecular forces (van der Waals force) to institute the merging of the interfaces. As shown in Fig. 2b, such merging occurs during the early stages of the penetration process. These types of merging are, thus, termed as early merging. This transitional boundary

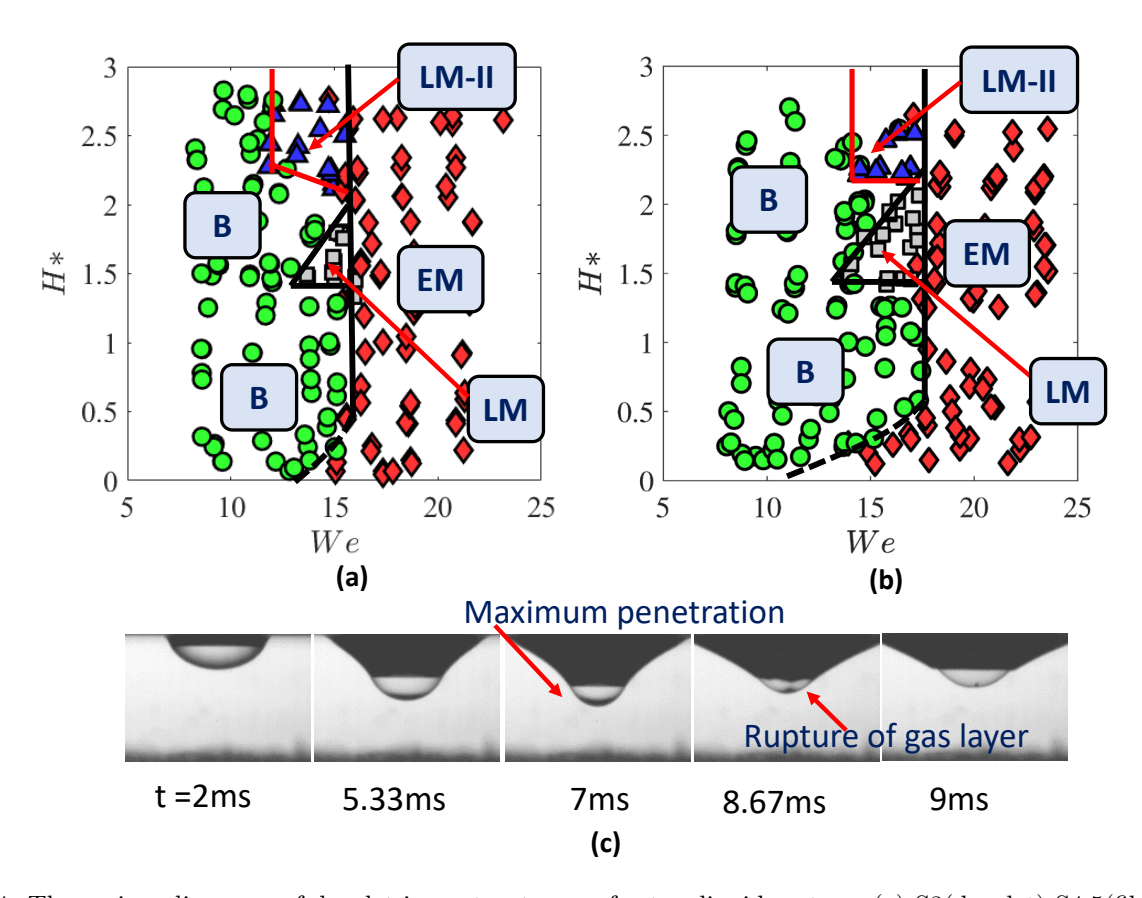


FIG. 4: The regime diagrams of droplet impact outcomes for two-liquid systems (a) S3(droplet)-S4.5(film), (b) S4.5(droplet)-S3(film). The transition boundaries between different impact outcomes are shown in black lines. B: Bouncing, EM: Early merging, LM: Late merging, LM-II: Late merging-II. (c) Side view observed in the experiment in a two-liquid system about the late merging-II.

between bouncing-to-merging at the critical We is called *inertial limit*, which is represented by a constant We line,  $We = We_{c,IL}$ , for large  $H^*$  (See regime diagrams in Fig. 3). At low  $H^*$ , the penetration process gets restricted by the bottom substrate, which provides additional support to squeeze the gas layer. Thus, merging can be achieved with lower impact kinetic energy or We. This transition is called *thin film limit* (TFL). Since the effect of the bottom substrate amplifies with a decrease in  $H^*$ , the critical We for merging ( $We_{c,TFL}$ ) also decreases. It is to be noted that the driving mechanism behind the bouncing-to-merging transition in both these limits (IL and TFL) is the droplet impact kinetic energy, and hence they are inertia-controlled.

In small We regime ( $We < We_{c,TL}$  or  $We < We_{c,TFL}$ ), when  $H^*$  is smaller than a critical value (1.5 for S3-S3 and 1.7 for S4.5-S4.5), the impact results in bouncing. In this regime with smaller film thickness, the droplet penetrates the film during the approaching stage and spreads on the substrate as shown in Fig. 2c. The degree of deformation in film and the droplet during the approaching stage in this regime is markedly different than that at high  $H^*$  (shown in Fig. 2a). Nevertheless, in the rebounding stage, the droplet and the film remain separated, and bouncing is achieved. However, when  $H^*$  is greater than the critical value, in the rebounding stage, the film relaxes faster than the droplet, asserting additional stress to the interracial gas layer, leading to merging. The merging in this regime occurs at a later stage of the impact (rebounding process) and is, thus, termed as late merging. The dynamics of the rebounding process are controlled by relative deformation in droplet and film, which is primarily affected by  $H^*$ . Thus, this bouncing-to-merging transitional line is given by a constant  $H^* = H^*_{c,DT}$  line, as shown in Fig. 3.

The mechanism mentioned above of *late merging* requires the droplet to penetrate to the bottom of the substrate. However, when  $H^*$  becomes so large that it exceeds the maximum penetration depth of the droplet, bouncing is reinstated. This transitional boundary, called *deep pool limit* (DPL) is expressed by the  $H^* = H^*_{p,m}$ . Here  $H^*_{p,m}$  is the normalized maximum penetration depth (shown in Fig. 2a) which depends on impact kinetic energy or We. All the transitional boundaries and bouncing and merging zones can also be seen in the regime diagrams (Fig. 3).

### 2. Two-Liquid System

Next, we will discuss the regime diagrams obtained for binary or two-liquid systems. Using alkanes and silicon oils listed in Tab. I, we have created a total of five combinations of binary/two-liquid systems, C10(droplet)-C14(film), C14-C10, S3-S4.5, S4.5-S3, and S3-S20. We expect the asymmetry in droplet and film properties will affect the impact dynamics. Indeed, we observed that the two-liquid systems show a richer regime diagram compared to that of a singleliquid system. Here we will only discuss the regime diagrams for two systems, S3-S4.5 and S4.5-S3 (shown in Fig 4a and b). The regime diagrams for the other three binary systems show similar behavior, and their regime diagrams are shown in the supplementary material. All three outcomes, bouncing, early merging, and late merging, observed for single-liquid systems, were also observed for two-liquid systems. The transitions, however, occur at different critical values compared to single-liquid systems as tabulated in Tab. II. Additionally, for two-liquid systems, we also observe an additional merging regime (late merging -II) at low Weber number ( $We < We_{IL,c}$ ) and large film thickness  $(H^* > H_{p,m}^*)$  conditions. A series of high-speed images for such merging is shown in Fig 4c. At this condition, where  $H^* > H_{p,m}^*$ , the film thickness is too large for the bottom substrate to affect the droplet penetration process. Moreover, since the initial kinetic energy is weaker  $(We < We_{IL,c})$ , the interfacial gas layer cannot be ruptured during the penetration process, and the droplet and film interfaces remain separated until the maximum penetration is achieved (Fig 4a, 7ms). The approaching stage of the two-liquid system resembles that of the single-liquid system in the same We and  $H^*$  range. However, in the rebounding stage, when the deformed film is retracting, we observe a sudden rupture in the gas layer for two-liquid systems (Fig 4a, 8.67 ms), instituting merging. Since this merging occurs at a very late stage of the impact, it is termed as late merging-II. At similar We and  $H^*$  conditions, droplets in single-liquid systems did not display such merging. Since late merging-II occurs only for binary systems but not for single-liquid systems, it is caused by the mismatch in properties between the droplet and the film. However, the side-view images confirm that the global morphologies are not significantly different between single and binary liquid systems. Thus, we expect the local gas layer dynamics to play a critical role in this new type of merging. Measurement of gas layer dynamics is rather complex and beyond the current experimental setup's capability; hence, it will be a topic of our future study.

	Droplet-Film	$We_{cr}$ (IL)	$H^*$ (DT)
	C10-C10	13.5	1.1
Alkanes	C14-C14	17	1.4
Aikanes	C14-C10	13	0.96
	C10-C14	9.3	0.85
	S3-S3	18	1.5
	S4.5-S4.5	20	1.76
Silicon Oils	S3-S4.5	16	1.4
	S4.5-S3	17.5	1.45
	S3-S20	18.3	-

TABLE II: Critical values for transitional boundaries in regime diagram for various single and two-liquid systems.

IL: Inertial Limit and DT: Deformation Transition.

### B. Effect of Asymmetry in Liquid Properties

In this section, we will revisit the physical mechanisms which control the various bouncing-to-merging transitions and derive scaling for them in the context of two-liquid systems. Experimentally, we observed that the trends in shifting of the transition boundaries in the regime diagrams for two-liquid systems are not simple functions of ratios of droplet and film properties. Our following analysis will show that a complex non-linear relationship governs the impact outcomes in two-liquid systems. Thus, a scaling analysis is needed to explain these phenomena.

### 1. Initial Limit

The early merging occurs early at the penetration stage of the impact, particularly for high  $H^*$  conditions. Thus, the inertial limit involves penetration of the droplet in the liquid film and large deformation in the film, as shown in Fig. 2b. To analyze this early stage of penetration, we can start with the energy balance between the two states, (1)

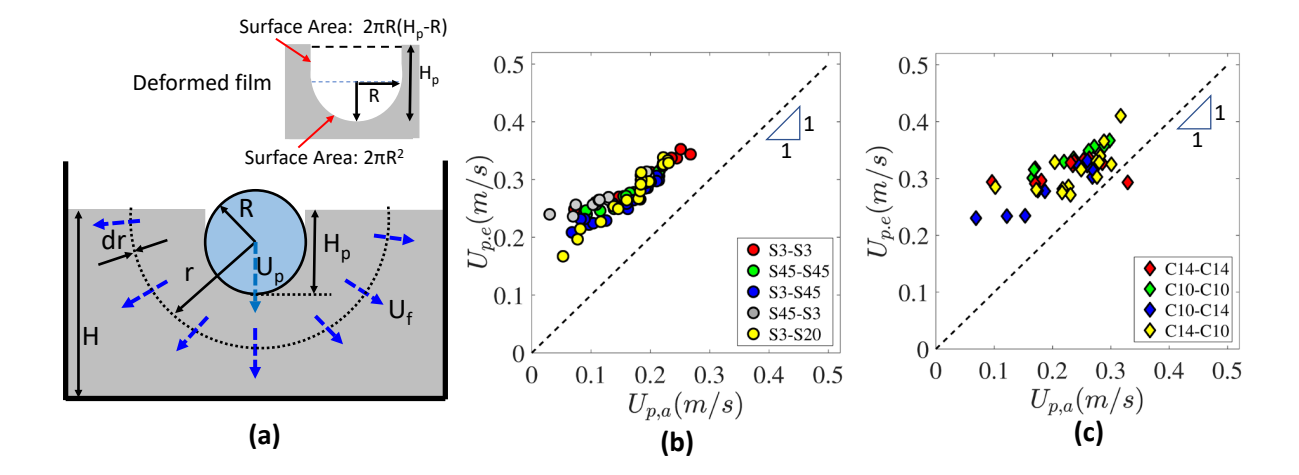


FIG. 5: (a) Schematic of the film deformation and flow in film, during the early penetration stage. Inset: shape of the deformed film and corresponding surface areas.

(b, c) Comparison between the penetration velocity from analysis  $(U_{p,a})$  and experiment  $(U_{p,e})$  for (b) silicon oils and (c)

before the impact and (2) at any point during the early penetration,

$$E_{kd,0} = E_{kd,p} + E_{kf,p} + (\Delta SE)_f + E_{\phi,f}. \tag{1}$$

Here, the initial kinetic energy of the droplet before the impact is  $E_{kd,0}=\frac{2}{3}\rho_d\pi R^3U^2$ .  $E_{kd,p}$  and  $E_{kf,p}$  are the kinetic energy of the droplet and film during the penetration.  $(\Delta SE)_f$  and  $E_{\phi,f}$  are the additional surface energy and viscous dissipation in the film. Here, we neglected the deformation in the droplet as it is minimal compared to the deformation in film. [25] Moreover, at the early stage of penetration, we can also assume that the flow field inside the droplet is uniform as there is no deformation. Thus, we can neglect the velocity gradient and the viscous dissipation inside the droplet. We can express  $E_{kd,p}=\frac{2}{3}\rho_d\pi R^3U_p^2$ , where  $U_p$  is the instantaneous penetration velocity of the droplet. To estimate the kinetic energy in the film, we consider the hemispherical radial flow induced by the penetrating droplet as shown in the schematic (Fig. 5a). From mass conservation, the velocity in the film at a radial distance r is  $U_f \approx U_P R^3/r^3$  [25, 41]. Hence, the total kinetic energy in the film can be calculated as,  $E_{kf,p} = \int_R^\infty 2\pi \rho_f r^2 U_f^2 dr \approx 2\pi \rho_f U_p^2 R^3$ . We note that the ratio of kinetic energy in the droplet and the film during the penetration process is  $E_{kd,p}/E_{kf,p} \approx (1/3)(\rho_d/\rho_f)$ . This implies that for a single-liquid system  $(\rho_d = \rho_f)$ , the kinetic energy of the film is three times that of the droplet  $(E_{kd,p}/E_{kf,p} \approx 1/3)$ , which was indeed observed in the experiments reported in our previous work [25].

The increase in surface energy  $(\Delta SE)_f$  arising from the deformation in film, can be calculated from the geometric considerations. For simplicity, here we assume a cylindrical geometry for the deformed film, as shown in the inset of Fig. 5a. This leads to  $(\Delta SE)_f \approx \sigma_f \left[2\pi R (H_p - R) + 2\pi R^2 - \pi R^2\right]$ , which can be further simplified to  $(\Delta SE)_f \approx \sigma_f \pi R (2H_p - R)$ . The total viscous dissipation loss until the merging event can be evaluate as  $E_\phi = \int_0^V \int_0^{t_m} \phi dV dt \approx \phi V t_m$ , where  $\phi$  is the local viscous dissipation rate, V is the volume and  $t_m$  is the time at which merging occurs. We can consider a boundary layer with thickness,  $\delta$ , around the deformed film surface where the viscous loss is concentrated. This leads to an effective volume of  $V \approx 2\pi R (H_p + R)\delta$ . The local dissipation rate can be evaluated based on the velocity gradient,  $\phi \approx \mu_f (\partial u_r / \partial r)^2 \approx (\rho_f \nu_f) (U_p / \delta)^2$ . The boundary layer thickness scales with the viscous penetration depth,  $\delta \sim \sqrt{\nu_f t_m}$ . It is to be noted that for low viscosity liquids or small Ohnesorge number (Oh) conditions, the viscous loss in the film  $(E_{\phi,f})$  becomes weak compared to the other terms in Eq. 1. However, we intended to perform the analysis for a general case, and thus, we did not make such an assumption. When we substitute the values of various energies in Eq. 1, we arrive at an expression for the penetration velocity

$$U_{p,a} \approx \sqrt{\frac{\rho_d R^2 U^2 - 3\sigma_f (2H_p - R)}{\rho_d R^2 + 3\rho_f R^2 + 3\rho_f (H_p + R)\sqrt{t_m \nu_f}}}$$
(2)

It is to be noted that the above expression is derived for the early penetration stage and is not valid when the droplet approaches maximum penetration depth. The latter will be discussed in the context of the *deep pool limit*. By using the impact velocity, merging depth, and merging time from individual experiments in Eq. 2, we can calculate the

analytical penetration velocity  $U_{p,a}$ . Moreover, by assuming a constant average velocity of penetration for the droplet, we can estimate an experimentally measured penetration velocity  $U_{p,e}$ , for both merging and non-merging cases:

$$U_{p,e} \approx \frac{H_p}{t_p} \tag{3}$$

Here,  $H_p$  is the penetration depth, and  $t_p$  is the time taken for the droplet to reach that depth. In Figs 5b (silicon oils) and 5c (alkanes), we compared the above-mentioned analytical penetration velocity  $(U_{p,a})$  with the experimentally measured averaged penetration velocity  $(U_{p,e})$ . We observe almost a linear relation with a slope close to 1, suggesting a good match between the scaling and the experimental data.

The early merging occurs for conditions where the penetration velocity becomes larger a critical value (Tab. III). The determination of the exact value of this critical velocity involves the evolution of the interfacial gas layer [24] and is beyond the scope of this study.

TABLE III: Critical averaged penetration velocity for early merging

							S4.5-S4.5		
l	$U_{p,e}(m/s)$	0.301	0.278	0.202	0.241	0.245	0.240	0.204	0.236

### 2. Deformation Transition Limit

Deformation Transition identifies the boundary across which the impact outcome changes from bouncing to late merging in the same impact We with an increase in  $H^*$  (Figs. 3 and 4). As discussed before, such a transition from bouncing to merging occurs in the rebounding stage, i.e. when the deformed droplet and film start to relax. During this process, the excess surface energy stored in the deformed droplet and the deformed film convert to kinetic energies associated with their corresponding rebounding (upward) motions. It can be hypothesized that the merging will occur if the upward velocity of the film  $(u_f)$  exceeds that of the droplet  $(u_d)$ , i.e.,  $u_f > u_d$ , as the film will catch the droplet. A simplified scaling for the single-liquid system has been demonstrated in our previous work [25]. Since the properties of the film and the droplet are different, for a two-liquid system, the analysis becomes complex, and the previous simplified expressions can not be directly used. Thus, we will lay down the formulation for two liquid systems. We will define the ratio of two velocities as  $U^* = (u_f/u_d)$ . Phenomenologically, when  $U^*$  increases beyond a critical value, i.e., film moves faster than the droplet, late merging occurs. We also note that the kinetic energy for the rebounding state comes from the deformed surface energy, and as such, we can write

$$E_{k,d} \approx (\Delta SE)_d - E_{\phi,d},$$
  

$$E_{k,f} \approx (\Delta SE)_f - E_{\phi,f}.$$
(4)

Here,  $(\Delta SE)_d$  (and  $(\Delta SE)_f$ ) and  $E_{\phi,d}$  (and  $E_{\phi,f}$ ) are the additional energy stored in deformed surface and dissipation loss during rebounding stage for the droplet (and the film), respectively. The deformed surface area of the film can be evaluated from the experimental images (Fig. 6a) and assuming a simplified geometry for the deformed droplet and the film as shown in Fig. 6b. Here, we will assume that, at the maximum deformed state, the droplet and the film take a trapezoidal shape, where  $w_1$ ,  $w_2$ , and  $w_3$  denote the three characteristic radii (shown in Fig. 6b). For this geometry, the additional surface area for the film at the maximum deformed state can be estimated as,

$$\Delta A_f \approx \pi R^2 \left[ w_1^{*2} + (w_1^* + w_2^*) \sqrt{H^{*2} + (w_2^* - w_1^*)^2} \right], \tag{5}$$

where  $w_i^* = w_i/R$  is the normalized characteristic radii. If the deformed trapezoidal droplet has a height of  $H_d$  (shown in Fig. 6b), we can evaluate the additional surface area from the mass conservation and geometric constraint,

$$\Delta A_d \approx \pi R^2 \left[ w_1^{*2} + w_3^{*2} - 4 + (w_1^* + w_3^*) \sqrt{H_d^{*2} + (w_3^* - w_1^*)^2} \right], \tag{6}$$

By employing the volume conservation (i.e. before and after deformation, the droplet volume is fixed) and the geometric constraints, one can also express,  $w_3^* = \left[w_1^{*3} + 4\left(w_2^* - w_1^*\right)/H^*\right]^{\frac{1}{3}}$  and  $H_d^* = \left[H^*/(w_2^* - w_1^*)\right]\left[(w_1^{*3} + 4\left(w_2^* - w_1^*\right)/H^*\right]^{\frac{1}{3}} - w_1^*$ . For details please refer to the supplementary material.

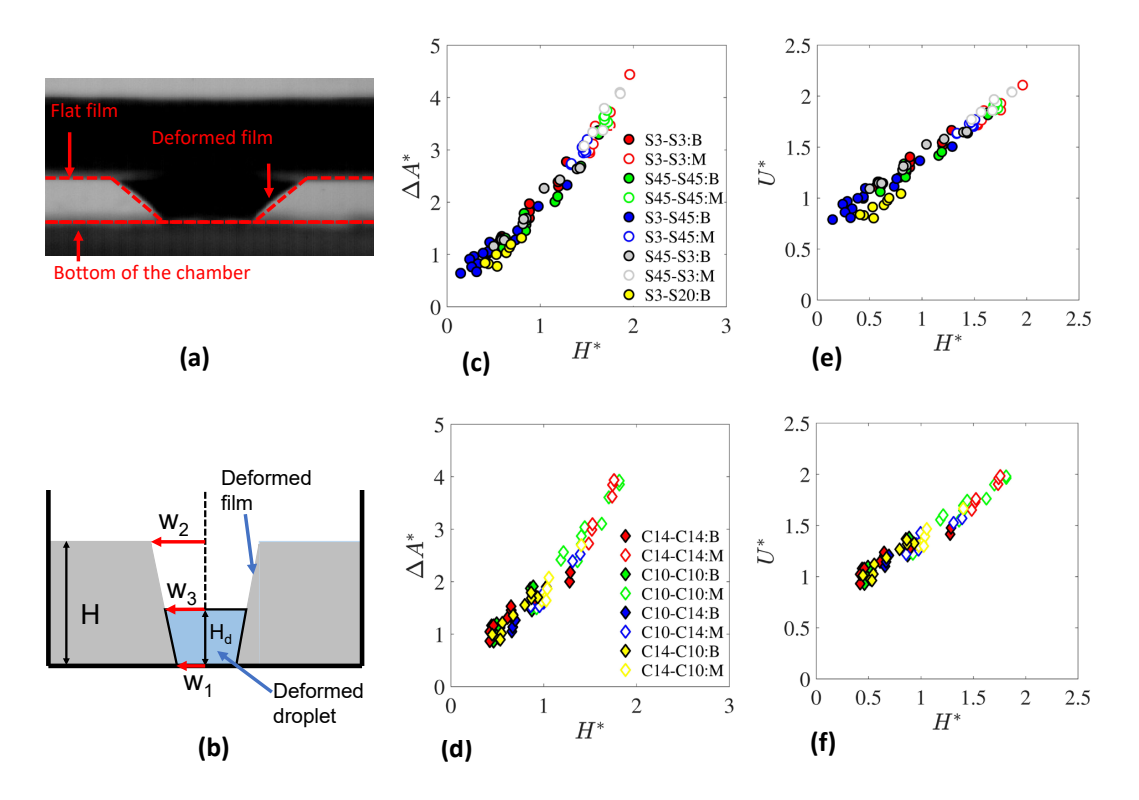


FIG. 6: (a) The side view of the impact process shows the film deformation at the maximum deformation state. (b)Schematic of the maximum spread deformation. (c, d) Relation between the area ratio  $(\Delta A^*)$  and the film thickness  $(H^*)$  for (c) silicon oils and (d) alkanes. (e, f) Relation between the rebounding velocity ratio  $(U^*)$  and the film thickness  $(H^*)$  for (e) silicon oils and (f) alkanes. In legends, B denotes bouncing, and M denotes merging outcomes.

Next, we evaluated the ratio of surface area,  $\Delta A^* = \Delta A_f/\Delta A_d$  from the experiments for various liquid systems at various We. They are plotted as a function of  $H^*$  in Figs. 6c (for silicon oils) and d (for alkanes). As we can observe, irrespective of We and the impact outcome (bouncing vs. merging), the area ratio  $(\Delta A^*)$  monotonically increases with  $H^*$ . Furthermore, by assuming that the relaxation processes of the deformed droplet and film surfaces are capillary controlled, we can estimate the viscous dissipation loss as  $E_{\phi} = E_0 \left(1 - e^{-2\eta \Delta t}\right)$ . Here,  $\eta = 8\nu/R^2$  captures the effect of viscosity.  $E_0$  is the initial energy in the system before the relaxation process. Hence, one can write  $E_0 \approx \Delta SE$ .  $\Delta t$  is the elapsed time in the rebounding process and taken to be a faction of the capillary time scale,  $\Delta t \approx t_{\rm cap} = C_{\rm cap} \left(\rho R^3/\sigma\right)^{1/2}$ , where  $C_{cap}$  is a proportionality constant. When substituted in Eq. 4, we get

$$E_{\phi,d} = E_{0,d} \left( 1 - e^{-2\eta_d \Delta t} \right) \approx (\Delta S E)_d \left( 1 - e^{-2C_{cap}Oh_d} \right),$$

$$E_{\phi,f} = E_{0,f} \left( 1 - e^{-2\eta_f \Delta t} \right) \approx (\Delta S E)_f \left( 1 - e^{-2C_{cap}Oh_f} \right)$$
(7)

Since the rebounding velocities are related to the kinetic energy by  $u_f \sim \sqrt{E_{k,f}/\rho_f}$  and  $u_d \sim \sqrt{E_{k,d}/\rho_d}$ , by substitution, one can find the velocity ratio  $U^* = u_f/u_d$  as

$$U^* \approx \sqrt{\left(\frac{\rho_d}{\rho_f}\right) \left(\frac{\sigma_f}{\sigma_d}\right) \left(\frac{e^{-2C_{cap}Oh_f}}{e^{-2C_{cap}Oh_d}}\right) \Delta A^*}$$
 (8)

Recognizing that  $A^*$  is primarily dependent on  $H^*$ , not We (Fig. 6c and d), we expect the velocity ratio ( $U^*$ ) to display similar dependence. Such behavior is indeed observed when plotted for various impact conditions in Fig. 6e (for silicon oils) and f (for alkanes). It is to be noted that the *late merging* occurs when the  $U^*$  increases beyond a critical value. From the figures, we can infer that the ratios of properties of the liquids have a weaker influence on  $U^*$  vs. We, confirmed by the collapse of data from all impact conditions on a single line. Since  $U^*$  depends on  $H^*$  (not We), the deformation transition (transition to late merging) occurs almost at a fixed  $H^*$  over a range of We for a given liquid system. However, the exact transitional value depends on the local dynamics of the gas layer and

TABLE IV: Critical velocity ratio for deformation transition

Liquid	C10-C10	C14-C14	C10-C14	C14-C10	S3-S3	S4.5-S4.5	S3-S4.5	S4.5-S3
$U_{crit}^*$	1.382	1.476	1.207	1.327	1.666	1.835	1.505	1.651

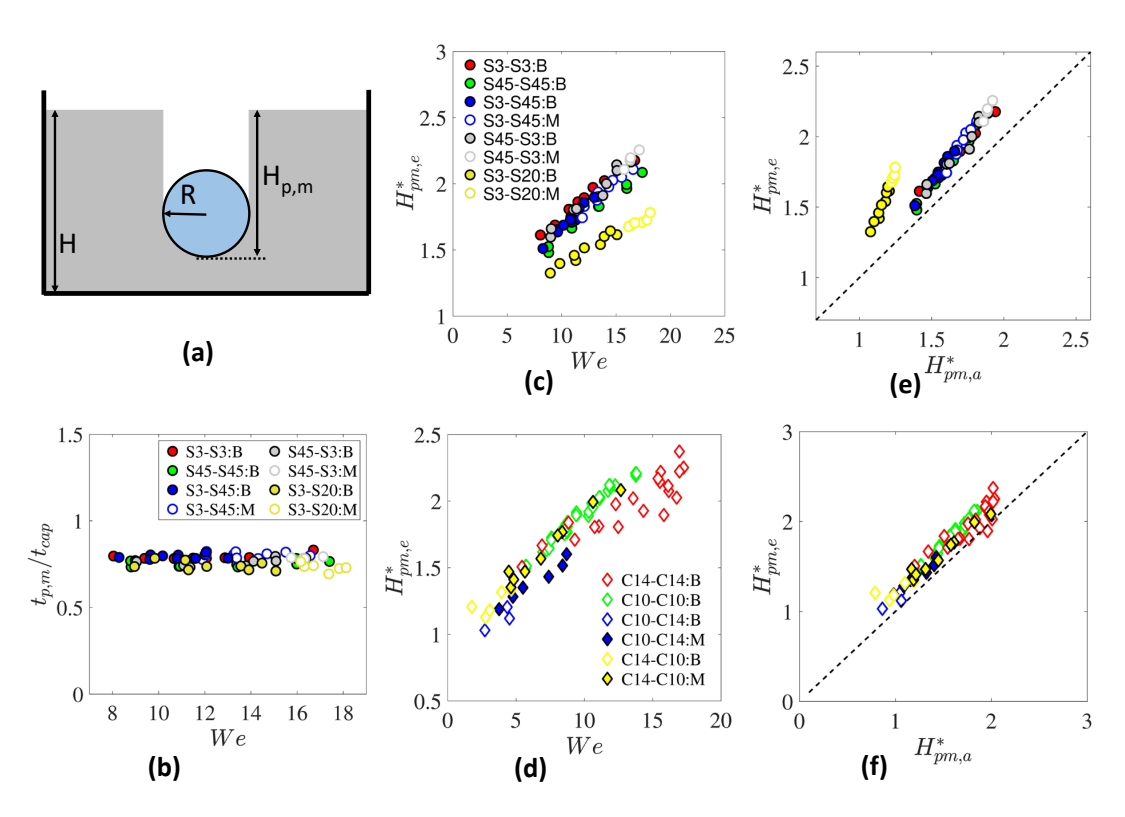


FIG. 7: (a) Schematic of the film deformation at the maximum penetration depth. (b) Penetration depth history with a normalized time scale in the deep pool for silicon oils. (c, d) Relation between the maximum penetration depth and the Weber number for (c) silicon oils and (d) alkanes. (e, f) Comparison between the maximum penetration depths from analysis  $(H_{pm,a}^*)$  and experiment  $(H_{pm,e}^*)$  for (e) silicon oils and (f) alkanes. In legends, B denotes bouncing, and M denotes merging outcomes.

hence, liquid properties as shown in table IV. We observe that the  $U_{crit}^*$  varies between 1.2 and 1.47 for hydrocarbon systems and between 1.5 and 1.83 for silicon oil systems.

#### 3. Deep Pool Limit

In the deep pool regime, where the film thickness (H) is greater than the maximum penetration depths  $(H_{pm})$ , the droplet cannot reach the bottom substrate during penetration. Thus, the substrate-assisted late merging cannot occur in this regime. The corresponding transitional boundary or deep pool limit can be expressed as  $H^* \approx H_{pm}^*$ , where  $H_{pm}^* = H_{pm}/R$  is the normalized maximum penetration depth, as shown in Fig. 2. When the penetration histories for impacts for several Wes and liquid-combination are plotted, one can see that the maximum depth  $(H_{pm})$  depends on both We and liquid properties (See Fig. 5c and d). In our previous work [25], we proposed a scaling analysis for a lower viscosity single-liquid system that shows that the maximum penetration depth changes almost linearly with Weber number, i.e.,  $H_{pm}^* \sim We$ . However, for two-liquid systems, the slope of  $H_{pm}^*$ -vs-We lines tend to change non-monotonically (Fig. 4) with liquid combinations. For example, the C10-C14 system displays a slope smaller than the corresponding single-liquid (C10-C10 and C14-C14) systems. Similar behavior was also observed for Silicon oil systems. We propose a modified scaling approach to identify the effects of two-liquid systems, which inherently includes the asymmetry in droplet and liquid properties.

As shown in the schematic in Fig. 7a, the penetration process involves significant deformation in the liquid film. Thus, we can hypothesize that the droplet's initial kinetic energy has been converted to surface energy at the maximum

penetration and the viscous dissipation.

$$E_{kd,0} = (\Delta SE)_f + (\Delta SE)_d + E_{\phi,d} + E_{\phi,f}$$

$$\tag{9}$$

The initial kinetic energy of droplet is  $E_{kd,0} = \frac{2}{3}\rho_d\pi R^3U^2$ . In our recent study [42] we showed that the deformation in a droplet impacting a film with large  $H^*$  is about 20% and significantly smaller than the deformation in the film. Thus, for simplicity, in the deep pool regime, we neglect the deformation in the droplet,  $(\Delta S_E)_d \approx 0$  and assume a cylindrical shape for the deformed film, as shown in the schematic (Fig. 7b). The additional surface area in the deformed film, then, can be expressed as  $(\Delta SE)_f \approx \sigma_f \pi R (2H_{pm} - R)$ .

The viscous dissipation in liquid film can be assumed to be restricted within a boundary layer (thickness:  $\delta_f$ ) along the deformed interface. The total viscous dissipation in film, then, can be calculated using a similar expression used for the inertial limit,  $E_{\phi,f} = \int_0^{V_f} \int_0^{t_{p,m}} \phi_f V_f dt \approx \phi_f V_f t_{p,m}$ . Here,  $t_{p,m}$  is the time taken by the droplet to achieve maximum penetration. As shown in Fig. 7b, it is proportional to the capillary time of the droplet  $(t_{p,m}/t_{cap} \approx 1)$ , irrespective of the We and liquid system. Thus, the boundary layer thickness and corresponding volume can be expressed as  $\delta_f = \sqrt{\nu_f t_{cap}}$ , and  $V_f = (\Delta SE)_f \delta_f$ , respectively. The viscous dissipation rate in the boundary layer scales as,  $\phi_f \approx (\nu_f \rho_f) \left(U_P/\delta_f\right)^2$ . The viscous loss in the droplet spans in whole droplet volume due to shape deformation. This leads to  $E_{\phi,d} = \int_0^{V_d} \int_0^{t_{p,m}} \phi_d V_d dt \approx \phi_d V_d t_{p,m}$ , where  $V_d = (4/3)\pi R^3$ ,  $t_{p,m} \approx t_{cap}$  and  $\phi_d \approx (\nu_d \rho_d)(U_p/R)^2$ . It is to be noted that the velocity scale associated with the penetrating droplet is the penetration velocity  $U_p$ . This was already discussed in the context of inertial limit in the section III B 1. Substituting the expressions for  $(\Delta SE)_f$ ,  $E_{\phi,d}$  and  $E_{\phi,f}$  in Eq. 9, we find a scaling relation for maximum penetration depth.

$$H_{pm}^{*} \approx \frac{\left[\frac{1}{6} \left(\frac{\sigma_{d}}{\sigma_{f}}\right) - \frac{\pi}{3} \left(\frac{1}{1+3\frac{\rho_{f}}{\rho_{d}}}\right) \left(\frac{\sigma_{d}}{\sigma_{f}}\right) Oh_{d}\right] We}{1 + \frac{\pi}{2} \left(\frac{1}{1+3\frac{\rho_{f}}{\rho_{d}}}\right) \left(\frac{\sigma_{d}}{\sigma_{f}}\right) \left(\frac{\rho_{d}}{\rho_{f}}\right)^{-1} \left(\frac{v_{d}}{v_{f}}\right)^{-\frac{1}{2}} WeOh_{d}^{\frac{1}{2}} + \frac{1}{2}}$$

$$(10)$$

Here, the Ohnesorge number for the droplet is defined as  $Oh_d = \mu_d/\sqrt{\rho_d\sigma_d(2R)}$ . Equation 10 represents a scaling relation that shows how maximum penetration depth changes with impact conditions and liquid properties. This expression includes the asymmetry in the droplet and the film properties. For low-viscosity single-liquid systems, it was shown that the  $H_{p,m}^* \sim We$  [25]. For small  $Oh_d$  and  $\sigma_d = \sigma_f$ , we recover the same relation from Eq. 10. It is also noted that for high viscosity (or  $Oh_d$ ) binary liquid systems, the relation between  $H_{p,m}^*$  and We becomes non-linear. In Figs. 7e (for silicon oils) and 7f (for alkanes), we compared the experimentally measured  $H_{p,m}^*$  with the theoretically obtained values from Eq. 10. We notice that the scaling works reasonably well for most single- and two-liquid systems. The data for S3-S20 shows some deviations from the scaling analyses, which can be attributed to the high viscosity of S20. As discussed before, the viscous loss term, in this work, was modeled using a simple scaling argument based on linear order velocity gradient  $(U_p/\delta_f)$ . However, a largely deformed liquid film's internal flow structures are more complex. Thus the simplistic form of scaling used in this work induces some errors in viscous dissipation, particularly for high-viscosity liquids, such as S20.

### IV. CONCLUSION

In summary, we presented an experimental study to assess the effects of asymmetry in liquid properties in bouncing to merging transitions for droplets impacting liquid films. The experiments were conducted using two-liquid groups, alkanes and silicon oils. We compared the regime diagrams constructed by mapping the impact outcomes (bouncing and merging) in a We-vs.-  $H^*$  graph. For two-liquid systems, where the droplet impacted on a film composed of different liquids, displayed four regimes, namely bouncing, early merging, late merging, and late merging-II. On the contrary, the same experiments with single-liquid systems (droplet and film are composed of the same liquid) showed only the first three regimes. Subsequently, we explored the physical mechanisms which control the transitions among various regimes and derived corresponding scaling laws. The analyses showed that asymmetry in the properties could induce non-linear effects, which were mostly absent for single-liquid systems. Finally, we used the data from experiments with single and two-liquid systems to show that the derived generic scaling model captures both the dynamics.

#### SUPPLEMENTARY MATERIAL

Please refer to the supplementary material for the regime maps for two-liquid systems using alkanes. The supplementary material also provides a detailed geometric derivation for the deformation transition limit.

#### ACKNOWLEDGMENTS

This work was funded by internal grants from the Jacobs School of Engineering of UCSD and the US National Science Foundation (Award No. CBET-2145210).

#### DATA AVAILABILITY

The data can be made available upon reasonable request to the corresponding author.

- [1] M. Rein, Phenomena of liquid drop impact on solid and liquid surfaces, Fluid Dyn. Res. 12, 61 (1993).
- [2] M. Rein, The transitional regime between coalescing and splashing drops, J. Fluid Mech. 306, 145 (1996).
- [3] H. Zhao, A. Brunsvold, and S. T. Munkejord, Investigation of droplets impinging on a deep pool: transition from coalescence to jetting, Exp. Fluids **50**, 621 (2011).
- [4] E. Castillo-Orozco, A. Davanlou, P. K. Choudhury, and R. Kumar, Droplet impact on deep liquid pools: Rayleigh jet to formation of secondary droplets, Phys. Rev. E 92, 053022 (2015).
- [5] G.-J. Michon, C. Josserand, and T. Séon, Jet dynamics post drop impact on a deep pool, Phys. Rev. Fluids 2, 023601 (2017).
- [6] D. A. Weiss and A. L. Yarin, Single drop impact onto liquid films: neck distortion, jetting, tiny bubble entrainment, and crown formation, J. Fluid Mech. 385, 229 (1999).
- [7] S. T. Thoroddsen, The ejecta sheet generated by the impact of a drop, J. Fluid Mech. 451, 373 (2002).
- [8] R. D. Deegan, P. Brunet, and J. Eggers, Complexities of splashing, Nonlinearity 21, C1 (2007).
- [9] H. Ma, C. Liu, X. Li, H. Huang, and J. Dong, Deformation characteristics and energy conversion during droplet impact on a water surface, Phys. Fluids **31**, 062108 (2019).
- [10] N. E. Ersoy and M. Eslamian, Capillary surface wave formation and mixing of miscible liquids during droplet impact onto a liquid film, Phys. Fluids **31**, 012107 (2019).
- [11] M.-J. Thoraval, K. Takehara, T. G. Etoh, S. Popinet, P. Ray, C. Josserand, S. Zaleski, and S. T. Thoroddsen, von kármán vortex street within an impacting drop, Phys. Rev. Letts. 108, 264506 (2012).
- [12] A. Saha, Y. Wei, X. Tang, and C. K. Law, Kinematics of vortex ring generated by a drop upon impacting a liquid pool, J. Fluid Mech. 875, 842 (2019).
- [13] B. Ray, G. Biswas, and A. Sharma, Regimes during liquid drop impact on a liquid pool, J. Fluid Mech. **768**, 492–523 (2015).
- [14] H. Deka, B. Ray, G. Biswas, A. Dalal, P.-H. Tsai, and A.-B. Wang, The regime of large bubble entrapment during a single drop impact on a liquid pool, Phys. Fluids 29, 092101 (2017).
- [15] M.-J. Thoraval, K. Takehara, T. G. Etoh, and S. T. Thoroddsen, Drop impact entrapment of bubble rings, J. Fluid Mech. 724, 234 (2013).
- [16] N. Blanken, M. S. Saleem, C. Antonini, and M.-J. Thoraval, Rebound of self-lubricating compound drops, Sci. Adv. 6, eaay3499 (2020).
- [17] N. Blanken, M. S. Saleem, M.-J. Thoraval, and C. Antonini, Impact of compound drops: A perspective, Curr. Opin. Colloid Interface Sci. 51, 101389 (2021).
- [18] Y. Wei and M.-J. Thoraval, Maximum spreading of an impacting air-in-liquid compound drop, Phys. Fluids **33**, 061703 (2021).
- [19] S. Zhu, A. Kherbeche, Y. Feng, and M.-J. Thoraval, Impact of an air-in-liquid compound drop onto a liquid surface, Phys. Fluids 32, 041705 (2020).
- [20] A. L. Yarin, Drop impact dynamics: splashing, spreading, receding, bouncing..., Annu. Rev. Fluid Mech. 38, 159 (2006).
- [21] C. Josserand and S. T. Thoroddsen, Drop impact on a solid surface, Ann. Rev. Fluid Mech. 48, 365 (2016).
- [22] D. Beilharz, A. Guyon, E. Li, M.-J. Thoraval, and S. T. Thoroddsen, Antibubbles and fine cylindrical sheets of air, J. Fluid Mech. 779, 87 (2015).
- [23] D. W. Murphy, C. Li, V. d'Albignac, D. Morra, and J. Katz, Splash behaviour and oily marine aerosol production by raindrops impacting oil slicks, J. Fluid Mech. **780**, 536 (2015).
- [24] X. Tang, A. Saha, C. K. Law, and C. Sun, Bouncing drop on liquid film: Dynamics of interfacial gas layer, Phys. Fluids 31, 013304 (2019).
- [25] X. Tang, A. Saha, C. K. Law, and C. Sun, Nonmonotonic response of drop impacting on liquid film: mechanism and scaling, Soft Matter 12, 4521 (2016).
- [26] X. Tang, A. Saha, C. K. Law, and C. Sun, Bouncing-to-merging transition in drop impact on liquid film: Role of liquid viscosity, Langmuir 34, 2654 (2018).
- [27] K.-L. Pan and C. K. Law, Dynamics of droplet-film collision, J. Fluid Mech. 587, 1 (2007).
- [28] H. Zhao, A. Brunsvold, and S. T. Munkejord, Transition between coalescence and bouncing of droplets on a deep liquid pool, Int. J. Multiph. Flow 37, 1109 (2011).

- [29] J. Zou, P. F. Wang, T. R. Zhang, X. Fu, and X. Ruan, Experimental study of a drop bouncing on a liquid surface, Phys. Fluids 23, 044101 (2011), https://doi.org/10.1063/1.3575298.
- [30] Z. Wu, J. Hao, J. Lu, L. Xu, G. Hu, and J. Floryan, Small droplet bouncing on a deep pool, Phys. Fluids 32, 012107 (2020).
- [31] Z. He, H. Tran, and M. Y. Pack, Drop bouncing dynamics on ultrathin films, Langmuir 37, 10135 (2021).
- [32] S. Shin, M. Li, X. Wu, A. Saha, and J. Bae, Role of soft-gel substrates on bouncing-merging transition in drop impact on a liquid film, Soft Matter 17, 571 (2021).
- [33] Z. Che and O. K. Matar, Impact of droplets on immiscible liquid films, Soft Matter 14, 1540 (2018).
- [34] K. R. Langley and S. T. Thoroddsen, Gliding on a layer of air: impact of a large-viscosity drop on a liquid film, J. Fluid Mech. 878, R2 (2019).
- [35] B. Wang, C. Wang, Y. Yu, and X. Chen, Spreading and penetration of a micro-sized water droplet impacting onto oil layers, Phys. Fluids **32**, 012003 (2020).
- [36] C. Liu, M. Shen, and J. Wu, Investigation of a single droplet impact onto a liquid film with given horizontal velocity, Eur. J. Mech. B 67, 269 (2018).
- [37] J. Qian and C. K. Law, Regimes of coalescence and separation in droplet collision, J. Fluid Mech. 331, 59 (1997).
- [38] P. Zhang and C. K. Law, An analysis of head-on droplet collision with large deformation in gaseous medium, Phys. Fluids 23, 042102 (2011).
- [39] N. Wadhwa, P. Vlachos, and S. Jung, Noncoalescence in the oblique collision of fluid jets, Phys. Rev. Lett. 110, 124502 (2013).
- [40] M. Li, A. Saha, D. Zhu, C. Sun, and C. K. Law, Dynamics of bouncing-versus-merging response in jet collision, Phys. Rev. E 92, 023024 (2015).
- [41] T. Tran, H. de Maleprade, C. Sun, and D. Lohse, Air entrainment during impact of droplets on liquid surfaces, J. Fluid Mech. 726, R3 (2013).
- [42] X. Tang, A. Saha, C. Sun, and C. K. Law, Spreading and oscillation dynamics of drop impacting liquid film, J. Fluid Mech. 881, 859 (2019).